

Slabs in the lower mantle — results of dynamic modelling compared with tomographic images and the geoid

Bernhard Steinberger *

Institut für Meteorologie und Geophysik, Johann Wolfgang Goethe-Universität, 60323 Frankfurt am Main, Germany

Received 9 November 1998; accepted 1 November 1999

Abstract

The recent increase in resolution of tomographic images of the Earth's interior has enabled us to “see” slabs in the lower mantle. On the other hand, the distribution of slabs can be inferred from subduction history, using a dynamical model of mantle flow. Comparison of tomographic images with model results can help to distinguish between alternative models of subduction history, tomographic models, and mantle flow models and thus improve our understanding of the Earth.

Here, a simple dynamic model of subduction is used and some results are presented: Amounts and locations of subduction are inferred from published models of plate motion and plate boundaries for the past 120 Ma; the latter have been interpolated on 2 Ma time intervals. Mantle flow driven by the density anomalies corresponding to subducted slabs is calculated with the method of Hager and O'Connell for a viscosity structure that features an increase in viscosity from $4 \cdot 10^{20}$ Pa below the lithosphere to $4 \cdot 10^{22}$ Pa in the lower part of the lower mantle. Slabs are advected in the flow field.

In the model, slabs sink on average about 1700 km through the mantle during 100 Ma; however, the calculated average horizontal motion of slabs throughout most of the mantle is only about 600–700 km; for slabs that have sunk to the lowermost mantle it is about 1000 km. This is in accordance with the previously observed good correlation between subduction locations and lowermost mantle heterogeneities. Slabs sink fastest in regions with abundant subduction and little trench migration (e.g., below East Asia). In the lowermost mantle, predicted slab locations tend to lie in areas with high seismic velocities, however, there are large areas of fast seismic velocities where no slabs are predicted, and which therefore presumably correspond to earlier subduction. In some regions (e.g., below Japan), our model approximately reproduces the observed shape of the slab. In other regions, where the agreement is poor, the results can help to further constrain models of subduction history and associated mantle flow.

Additionally, the predicted geoid is computed and compared with the actual geoid. Predicted and observed geoid have similar magnitude and a number of features in common, however, an optimization of the fit is not attempted here, since, in order to do this, also the hot upwellings from the lower boundary layer (presumably in the form of plumes) would have to be included. © 2000 Elsevier Science B.V. All rights reserved.

Keywords: Subduction history; Slabs; Mantle flow; Geoid; Tomography

* Corresponding author. Fax: +49-69-798-23280.

E-mail address: steinber@geophysik.uni-frankfurt.de (B. Steinberger).

1. Introduction

The subduction of lithospheric slabs is one of the key ingredients in the theory of plate tectonics. In the upper mantle, the slabs can be located by the occurrence and distribution of deep earthquakes; however, there is no such direct evidence indicating the fate of subducted slabs after they reach the transition zone. Seismic tomography and the geoid can, however, give indication where the slabs will move to: It has been noted some time ago that there is a good correlation between fast seismic anomalies in the lower mantle and the locations of subduction zones during the Cenozoic and Mesozoic at low spherical harmonic degrees (e.g., Richards and Engebretson, 1992). More recent high-resolution tomographic images (e.g., Grand et al., 1997; van der Hilst et al., 1997) have shown fast seismic anomalies going from beneath subduction zones all the way to the core–mantle boundary, indicating that slabs do in fact sink through the entire lower mantle, perhaps after remaining in the transition zone for a while in some places.

The distribution of fast seismic anomalies in the lower mantle can therefore give important indications about both the locations of past subduction and about mass flow inside the mantle. To correctly interpret seismic anomalies in terms of subduction history and mantle flow, it is necessary to use a dynamic model of flow in the mantle. With such a model, the distribution of density anomalies inside the mantle (“slab model”) can be calculated for a given distribution of subduction in time and space (“subduction history model”). Density anomalies can be compared with seismic anomalies; a geoid can be predicted from the density anomalies and compared with the actual geoid. If the subduction history is well-known and the resolution of tomographic images is good, it can be attempted to constrain mantle flow and the parameters by which it is determined (especially viscosity) by optimizing the agreement between slab model and seismic anomalies. An acceptable fit to the geoid can serve as additional constraint. On the other hand, if subduction history is poorly known (especially for times older than around 120 Ma), tomographic images and the geoid, in combination with the flow model, can help to better constrain subduction history. Further-

more, predictions of seismic anomalies can be attempted in regions where seismic coverage is poor.

In the first paper on this subject, Gurnis (1993) used a model of subduction history, assuming vertical sinking of slabs, with sinking speed only depending on depth, to predict dynamic topography and hence, marine inundation of continents. He found that the predicted geographical pattern of flooding correlates well with the geological record. Ricard et al. (1993) showed that with a similar simple model, a remarkably good fit of both geoid and tomography can be achieved. The subject is reviewed by Lithgow-Bertelloni and Richards (1998). More recently, Bunge et al. (1998) used a spherical convection code with given plate motion boundary conditions to compute mantle density heterogeneities and compare them with seismic tomography. Using a similar approach, but focusing in more detail on a particular region and varying the plate reconstructions within uncertainty bounds consistent with the geologic record, Gurnis et al. (1998) discussed the Cretaceous vertical motion of Australia and the anomalously low topography of the Australian–Antarctic discordance. Their model inferred that a slab subducted East of the present location of Australia is presently being drawn up by the Southeast Indian Ridge. The scope of this work is similar to Bunge et al. (1998), but a somewhat different approach is used: We explicitly introduce slab particles at subduction zones; density heterogeneities inferred from slab distribution and flow field are evolved in a mutually consistent manner. Some implications on mantle flow and viscosity as well as subduction history are also discussed.

2. Numerical model of mantle flow and slab distribution

Essentially, the model uses the distribution of mass anomalies due to slabs to calculate a flow field, and the flow field in turn is used to calculate the motion of slabs. In this way, slabs are advected from their initial locations, as given in the “slab input model” to their present locations. This method is somewhat different from our previous work described in Steinberger and O’Connell (1998) in that the density heterogeneities driving mantle flow are not inferred from seismic tomography but from sub-

duction history itself. Anything else would be less than self-consistent: Whereas it is probably justified to treat plume conduits as passive features not influencing large-scale mantle flow, this is not possible for subducted slabs, which are considered a main driving force for large-scale mantle flow. To construct the slab model, a slab input model and a method to calculate mantle flow are therefore required. Both are described in the following.

2.1. *The slab input model*

Amount and distribution of subducted slabs are inferred from the model of plate motions and boundaries compiled by Lithgow-Bertelloni et al. (1993), which is based on Gordon and Jurdy (1986) for the Cenozoic. These sets of plate boundaries were interpolated at 2-Ma time intervals.

Using the interpolated sets of plate boundaries and the original sets of plate rotations, for each boundary segment the convergence rate orthogonal to the boundary is calculated. A slab “particle” is assigned to the boundary segment if the convergence rate for the boundary segment itself and at least one neighbouring boundary segment is larger than 0.55 cm/year. These conditions were found to be appropriate to characterize subduction zones, and to keep the number of “stray data points” small, which, e.g., result on transform faults of mid-oceanic ridges, if the calculated relative plate motion is not exactly parallel. Each particle is specified by location (latitude, longitude), time, and anomalous mass. Anomalous mass is the product of area and the depth integral of density anomaly. The area is the product of orthogonal convergence rate, length of the corresponding boundary segment and the time interval represented (2 Ma).

Using the theory of a cooling half-space, the depth integral of density anomaly as a function of lithospheric age is determined as:

$$\int \Delta \rho dz = 2 \rho_0 \alpha \Delta T \sqrt{\kappa \cdot \text{age} / \pi} \quad (1)$$

where ρ_0 is density, α is thermal expansion coefficient, ΔT is the temperature difference across the lithosphere and κ is thermal diffusivity. We use the numerical values $\rho_0 \alpha \Delta T = 103 \text{ kg m}^{-3}$ and $\kappa = 1.2$

$\cdot 10^{-6} \text{ m}^2 \text{ s}^{-1}$. This choice of parameters allows a good fit of the observed ocean floor topography back to about 100 Ma (Parsons and Sclater, 1977).

Lithospheric age at the subduction zones is calculated from the same models of plate motion and geometry if possible. If this age could not be determined, the estimated average age of lithosphere with undetermined age is used. Results do not depend much on assumed lithospheric ages and are rather similar even if a constant depth integral of density anomaly (corresponding to 100 Ma age) is assumed.

Computed particles corresponding to the India–Eurasia collision during the past 40 Ma are specifically excluded, however this has a rather negligible effect on the result. A kinematic approach is used to calculate the motion of slab particles in the uppermost mantle: It is assumed that (in the reference frame of the overriding plate) slabs continue to move at the same speed as the plate to which they are attached, but with a dip angle of 45° , until they reach a depth of 380 km. This depth is somewhat arbitrary and is chosen such that the buoyancy effects of the two-phase transitions can be included in the flow calculations. Results do not critically depend on the exact value of the dip angle assumed: Since a lateral displacement of a few hundred kilometers is not much at the global scale considered here, results look even broadly similar, if vertical sinking is assumed instead. The slab input model thus obtained is shown in Fig. 1. It consists of the locations, times at which they have reached a depth of 380 km, and masses of slab particles.

2.2. *Method to calculate mantle flow*

Starting at the locations and times specified in the slab input model, the slab particles are advected in mantle flow, which is calculated as follows: Anomalous masses of slab particles are distributed onto a grid of 32 points in latitude, 64 points in longitude and 47 radial points. For the latitudes, the points of the Gauss–Legendre quadrature formula are used; in longitude, the points are equally spaced. For each slab particle, the anomalous mass is distributed to the eight surrounding gridpoints such that the center of mass stays the same. By dividing anomalous mass by volume assigned to a gridpoint, a density anomaly is

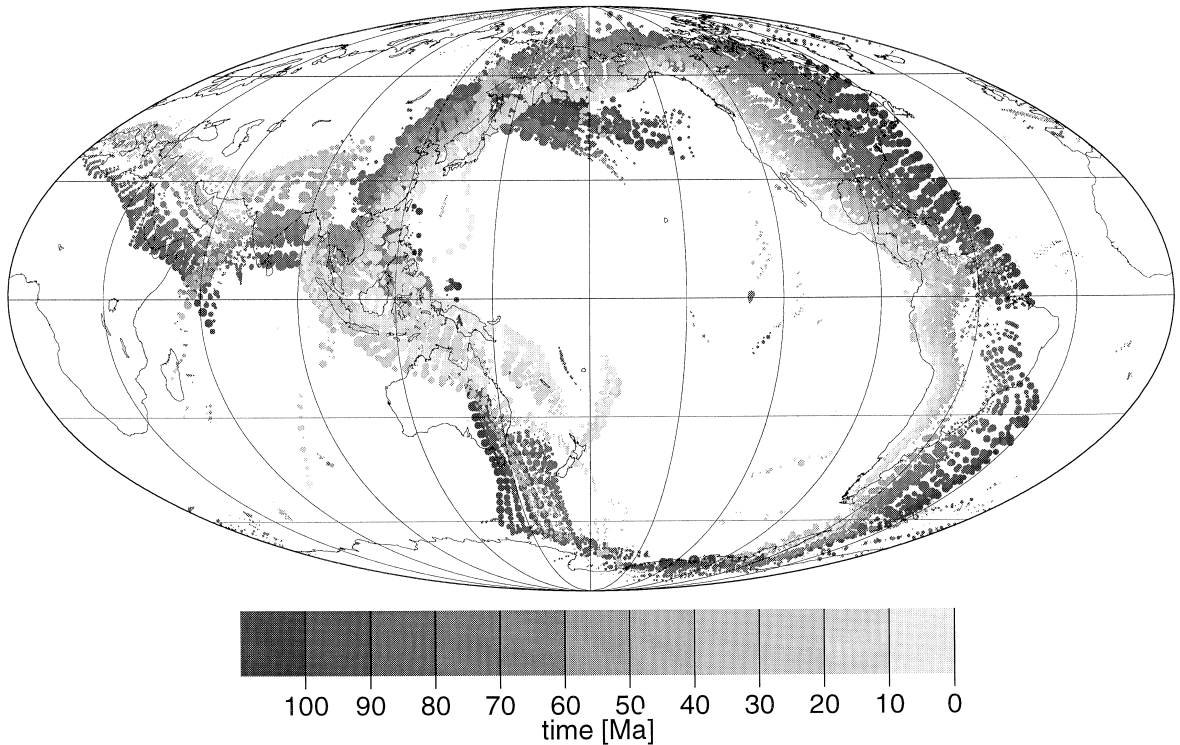


Fig. 1. Slab input model: The figure shows locations, times and masses of slab “particles” inserted into the mantle at a depth 380 km. It corresponds to the subduction history model shown in Steinberger and O’Connell (1998), which in turn is based on the data of Gordon and Jurdy (1986) and Lithgow-Bertelloni et al. (1993). Areas of dots correspond to masses of particles, however, overlap between dots occurs. See text for details on how slab input model was obtained.

calculated on the grid, and subsequently expanded in spherical harmonics up to degree and order 31. Spherical harmonic expansion is facilitated by the specific choice of gridpoints. After this, the method of Hager and O’Connell (1979, 1981) is used to calculate the flow field. This method essentially computes a spherical harmonic expansion of the flow field, given spherical harmonic expansions of the density field and surface plate motions, and a radial viscosity structure. A more detailed description of the method has been given by Steinberger and O’Connell (1998). (n.b.: There should be a minus-sign instead of a plus-sign in the third lines of Eqs. (A2) and (A3) of that paper. These equations were misprinted, but used correctly.)

Here, the original routines were modified to include the effects of compressibility and phase boundaries: The latter are included as mass sheets on the

undeflected boundary that correspond to the mass anomalies caused by the phase boundary deflection. Two phase boundaries (at depth 400 km with a product of Clapeyron slope and density jump $0.5 \cdot 10^3$ MPa/K kg/m^3 and at depth 670 km with $-0.3 \cdot 10^3$ MPa/K kg/m^3) are included. The value at 400 km is based on Akaogi et al. (1989) for a Pyrolite mantle with 60% Olivine content. The value at 670 km is given by Akaogi and Ito (1999). It is smaller than values assumed in many convection calculations, as it also includes the effects of the Majorite–Perovskite transition, which occurs at a similar depth with a positive Clapeyron slope. With these parameters, the effects of phase boundaries are found to be rather small, in agreement with the results by Bunge et al. (1998): They compared two convection simulations, one with rather strong phase boundaries and one without phase boundaries and found a better fit

to Grand’s model in the case without phase boundaries. Including compressibility does not have a large effect either.

Only slabs that have been subducted below 380 km are used to calculate flow. Since the motion of slabs above 380 km is calculated kinematically, it would be the most consistent approach to use the slabs as kinematic boundary conditions for the flow. However, this has not been done since the numerical implementation would take considerable effort. Moreover, since plate motions are already used as kinematic boundary conditions at the surface, mantle flow already has a downward component of magnitude similar to convergence rate below subduction zones. Thus, including subducted slabs as further boundary conditions would presumably not change results by much. Whether or not slabs in the uppermost 380 km are included in the flow calculation does not have much effect on the flow field in the lower mantle, hence on the results.

Anomalous masses of slab particles are assumed to decrease proportional to their radial coordinate (= Earth radius minus depth), thus approximately accounting for the decrease of thermal expansion coefficient with depth (Chopelas and Boehler, 1989). Results do not strongly depend on the exact depth dependence of anomalous mass chosen.

2.3. Viscosity structure

The method of Hager and O’Connell (1979, 1981) enables flow calculation for a viscosity varying with

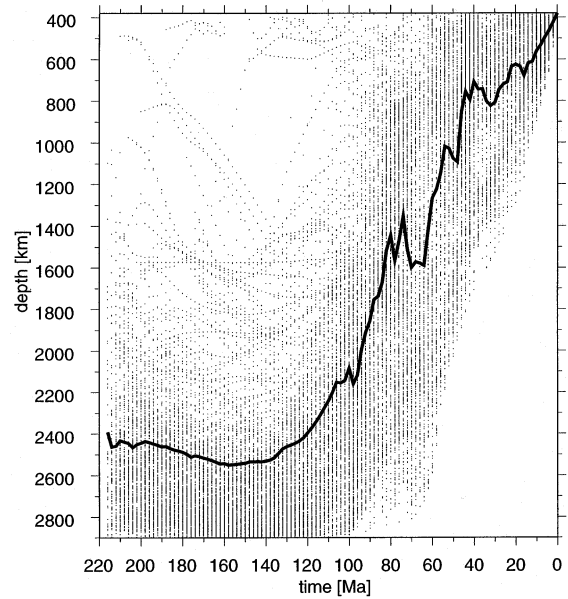


Fig. 3. Calculated present depth of slab particles vs. time of subduction (below 380 km). Each dot corresponds to one slab particle. The black line shows the average depth of slab particles for a given time of subduction.

radius only. The viscosity structure used here is shown in Fig. 2, and is the same as in Steinberger (2000), where it was discussed that it is in agreement with evidence from postglacial rebound and the geoid, and a review of this evidence was given. The relative values of lithospheric, asthenospheric and

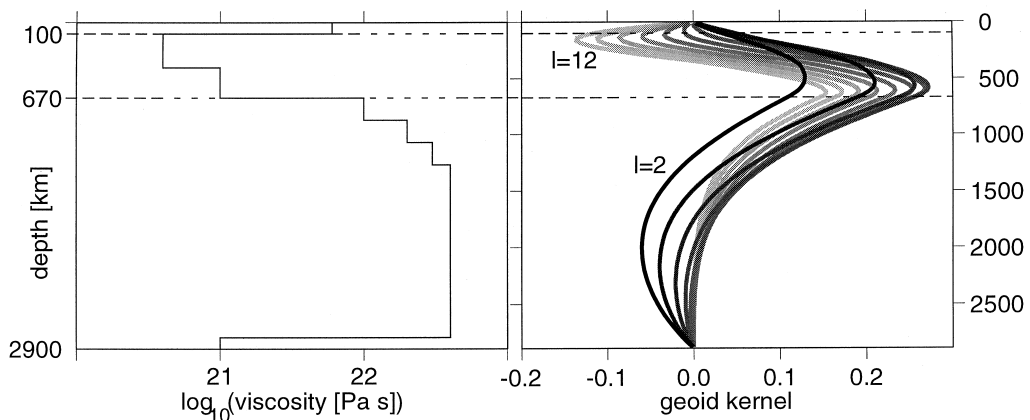


Fig. 2. Viscosity structure used, and corresponding geoid kernels (calculated for a free upper boundary with the method described by Panasyuk et al., 1996) for spherical harmonic degrees 2–12, graytone corresponding to degree.

lower mantle viscosity were especially chosen to allow an acceptable fit of the observed geoid; kernels are very similar to the viscosity structure for which Ricard et al. (1993) found an optimum fit of the geoid, using a similar, but somewhat simpler model of subduction. Specifically, geoid kernels that are significantly negative in the lower mantle are required to predict a geoid similar to the observed one.

Obviously, the neglect of lateral viscosity variations is one of the fundamental limitations of this and other studies on this subject. Lateral viscosity variations are, however, poorly known and difficult to implement numerically (e.g., Gurnis et al., 1998). Moreover, like the sinking speed of a viscous sphere that is mostly determined by the viscosity of the surrounding fluid, it can be expected that the sinking speed of slabs depends mostly on ambient mantle viscosity and not so much on the internal slab rheol-

ogy, in which case the use of a viscosity structure varying with radius only would be reasonable.

2.4. Motion of slab particles in mantle flow

In principle, the motion of slabs can be calculated by simply interpolating the flow field from the grid to the locations of the slab particles. However, the model of plate boundaries used starts at 120 Ma, whereas in the real Earth, there has been subduction for much longer. Therefore at early times our slab model would significantly underpredict flow speeds and the calculated slab sinking speed would be too slow. To compensate for this, and to obtain a more realistic initial condition, we start the calculation 220 Ma ago, with constant subduction locations for the first 110 Ma, similar to Bunge et al. (1998). When discussing the distribution of slabs, inferred density

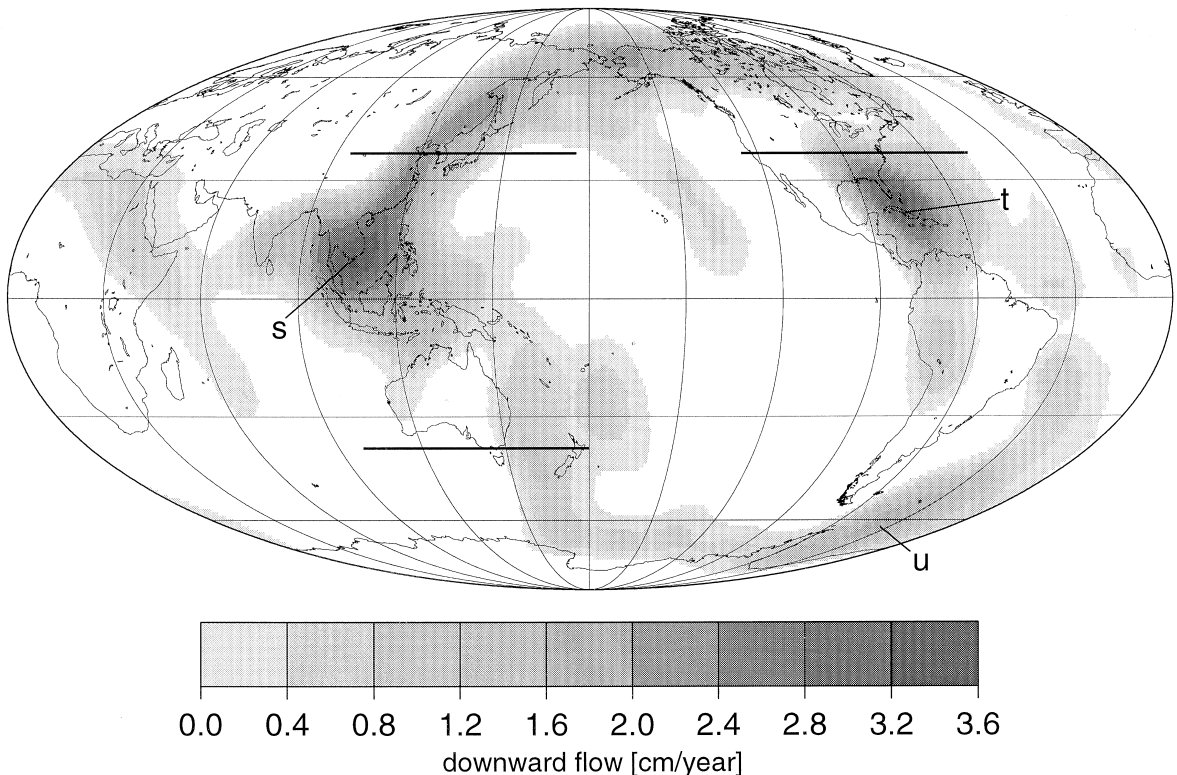


Fig. 4. Calculated vertical flow component at depth $0.72r_E$. Downward flow only is shown. Thick black lines indicate locations of cross sections shown in Figs. 7–9. Letters (s,t,u) indicate places mentioned in the text.

distribution and comparison with tomography and the geoid (i.e., for the results displayed in Figs. 5–11), we will however only use slabs inserted after 120 Ma, which are based on an actual plate motion history model.

3. Results of mantle flow and slab distribution

3.1. Sinking speed of slabs

The previously found good correlation between lowermost mantle seismic heterogeneity and Cenozoic and Mesozoic subduction history (e.g., Richards and Engebretson, 1992) suggests that slabs take of the order of 100 Ma to sink to the lowermost mantle. Our results are in accordance: Fig. 3 shows that slabs that have been subducted 120 Ma ago or earlier have sunk to within a few hundred kilometers of the CMB on average. The average depth of slabs subducted

later than 120 Ma as a function of subduction time indicates an average sinking speed of the order of $2000 \text{ km}/120 \text{ Ma} \approx 1.7 \text{ cm/year}$. This value is probably slightly over-estimated, because a constant subduction location prior to 110 Ma was assumed, and in this case, sinking speeds tend to be higher than in the case of rapid trench migration, as will be discussed below. Calculations for a variety of other models (with different viscosity structures, phase boundary parameters, thermal expansivity, etc.) yielded rather similar results. The largest uncertainties arise from the rather poor knowledge of lower mantle viscosity, which might be a few times higher or lower, but even so, comparison of various model results indicate uncertainties in average sinking speed of a few tens of percent at most.

Lateral variations of sinking speed are, however, much larger, and thus need to be considered when comparing predicted density anomalies with results from seismic tomography. Fig. 4 shows the vertical component of the mantle flow field at a depth halfway

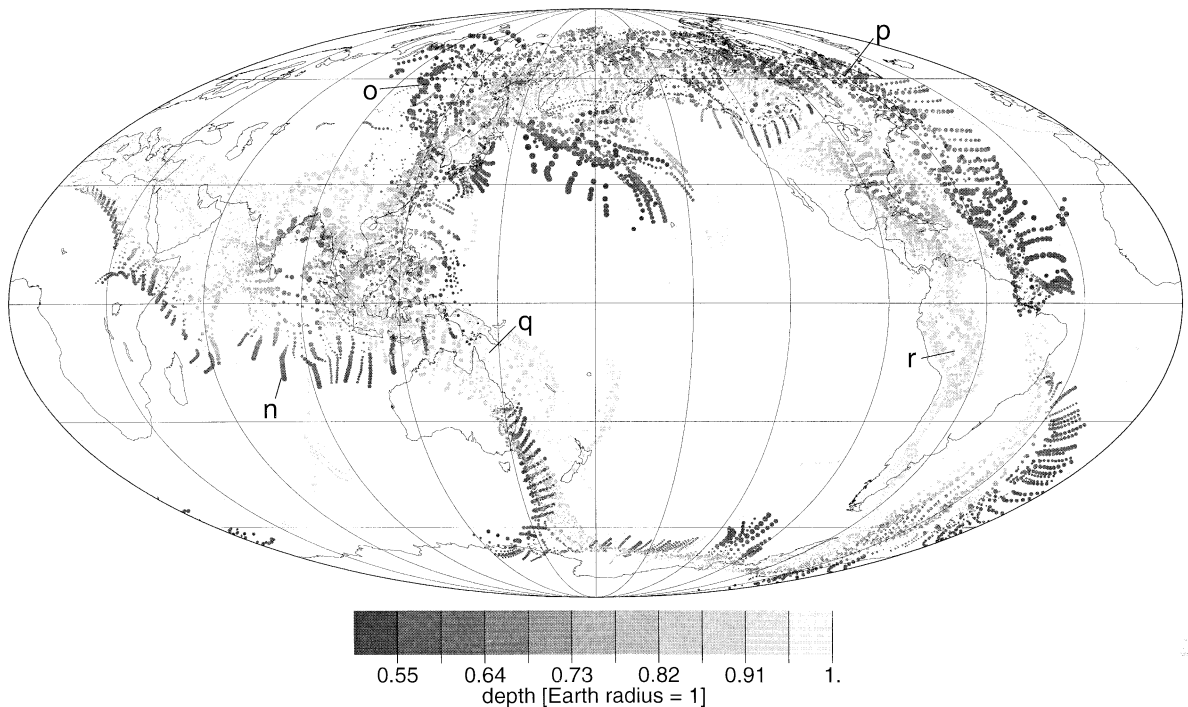


Fig. 5. Calculated present distribution of slabs. Areas of dots correspond to masses of particles, however overlap between dots occurs. Letters (n,o,p,q,r) indicate places mentioned in the text. Only slabs that have been inserted into the mantle below 380 km depth are plotted.

between transition zone and CMB: The maximum sinking speed is about twice the average slab sinking speed inferred from Fig. 3. Correspondingly, the fastest sinking slabs reach the lowermost mantle

after only about 60 Ma, as can also be seen in Fig. 3. High sinking speeds tend to occur in regions with large amounts of subduction and little trench migration.

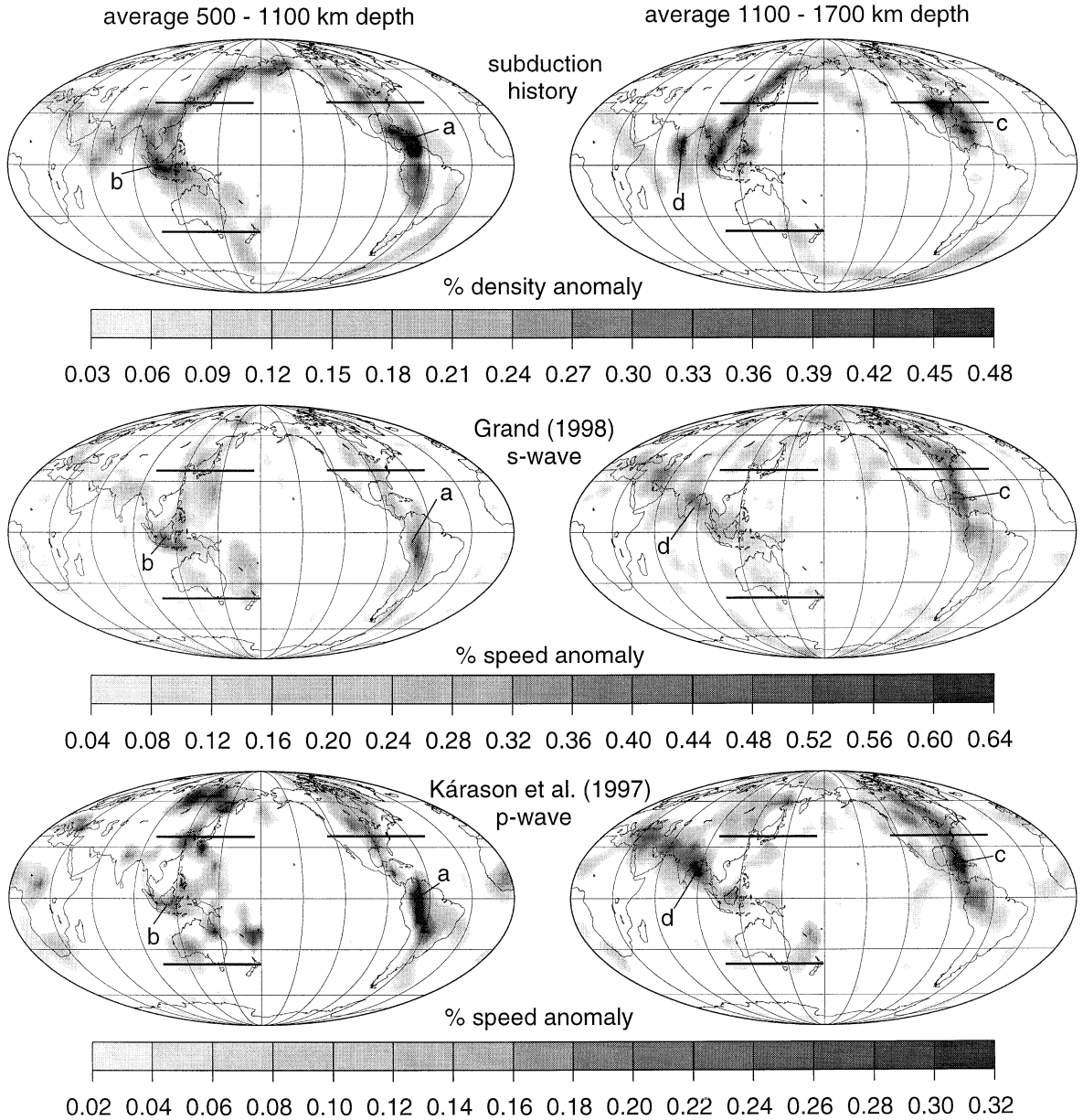


Fig. 6. Predictions of density anomalies in the mantle from subduction history compared with tomographic models — depth averages of four different mantle depth intervals. Only positive anomalies are shown. Thick black lines indicate locations of cross-sections shown in Figs. 7–9. Letters (a,b,c,d,e,f,v,w) indicate places mentioned in the text.

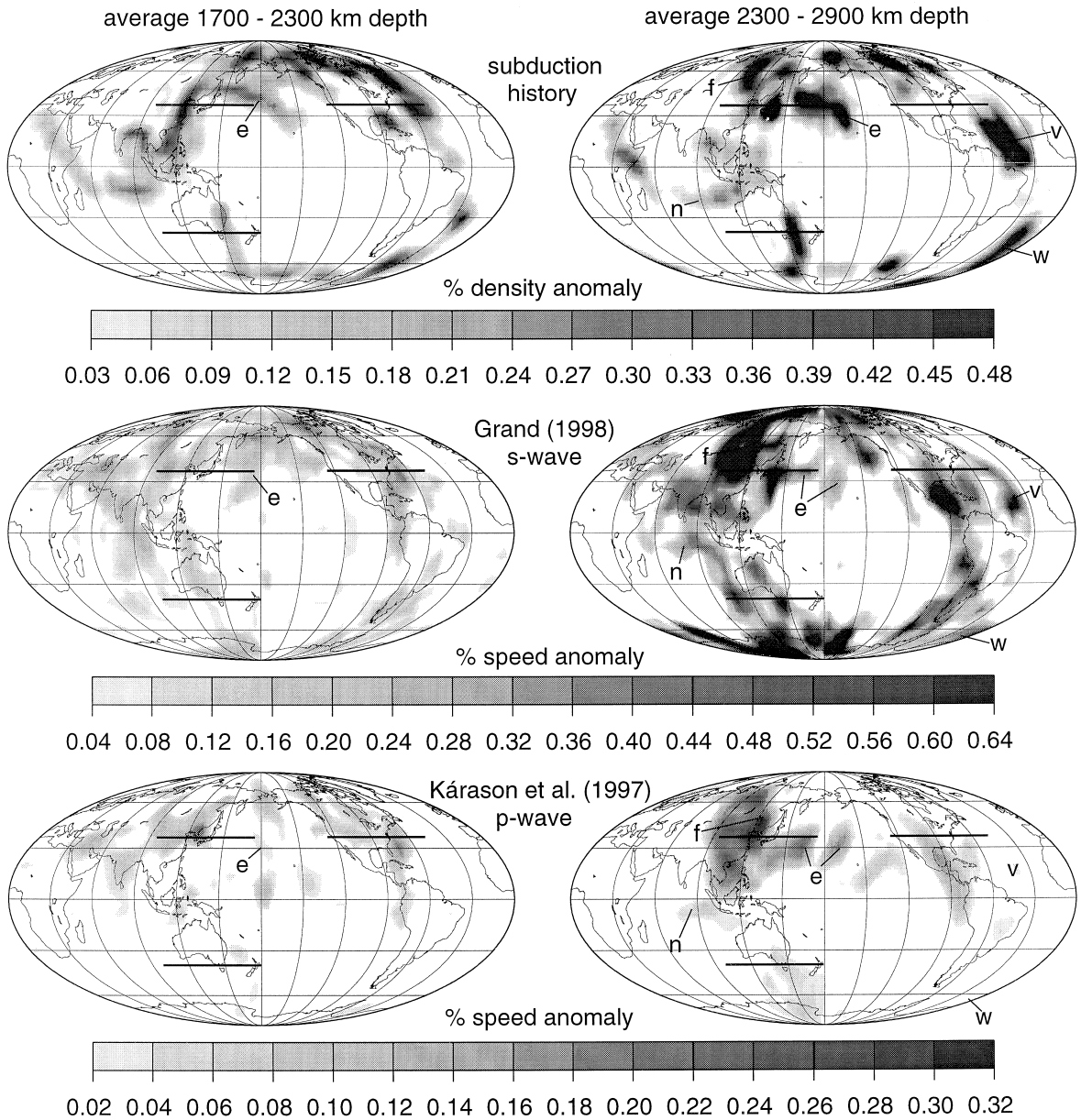


Fig. 6 (continued).

3.2. Magnitude and lateral distribution of density anomalies due to slabs

Fig. 5 shows the calculated present distribution of slabs: in order to compare results with tomographic models of wave speed, it is however more useful to

compute the corresponding density field: Because of the uncertainties in our model parameters, hence slab sinking speed, slab locations may be predicted somewhat too deep or too shallow. It is therefore more appropriate to compare not at given depth levels, but averaged over certain depth intervals: In Fig. 6, the

mantle is divided in four intervals spanning 600 km each. The p-wave model of Káráson et al. (1997), and the latest s-wave model by S. Grand (1998, pers. comm.), which is similar to Grand et al. (1997) are used for comparison. These models were chosen because of their high resolution, but the choice does not imply judgment regarding the quality of any model. These models were converted from the original grid to spherical harmonic coefficients and subsequently re-evaluated in space domain, using coefficients up to degree and order 31, as for the slab model.

The computed magnitude of the density anomalies is up to about 0.5% in the upper three layers and somewhat larger in the lowermost mantle. For comparison, below 500 km depth the anomalies of the s-wave model have similar magnitude (except in the lowermost mantle, where they are larger), the anomalies of the p-wave model are even smaller. Based on mineral physics arguments, however, relative density anomalies should be of the order of 0.2–0.3 times relative s-wave speed anomalies, or 0.4–0.5 times relative p-wave anomalies (e.g., Karato, 1993), indicating that either the anomalies of the tomographic models are too small or the predicted density anomalies are too large. Compared to other tomographic models, (e.g., Su et al., 1994; Li and Romanowicz, 1996) the amplitude of the models by Grand (1998) and Káráson et al. (1997) is indeed somewhat low.

In the uppermost layer (500–1100 km), the predicted density anomaly in most places represents the recent subduction history, with positive anomalies in the regions surrounding the Pacific, and in an area stretching from the Mediterranean to Indonesia, corresponding to the former Thetys subduction. Most of the positive velocity anomalies of the seismic models are also in these regions. The models also agree in some of the details: all three models show an elongated anomaly stretching through the Americas, with

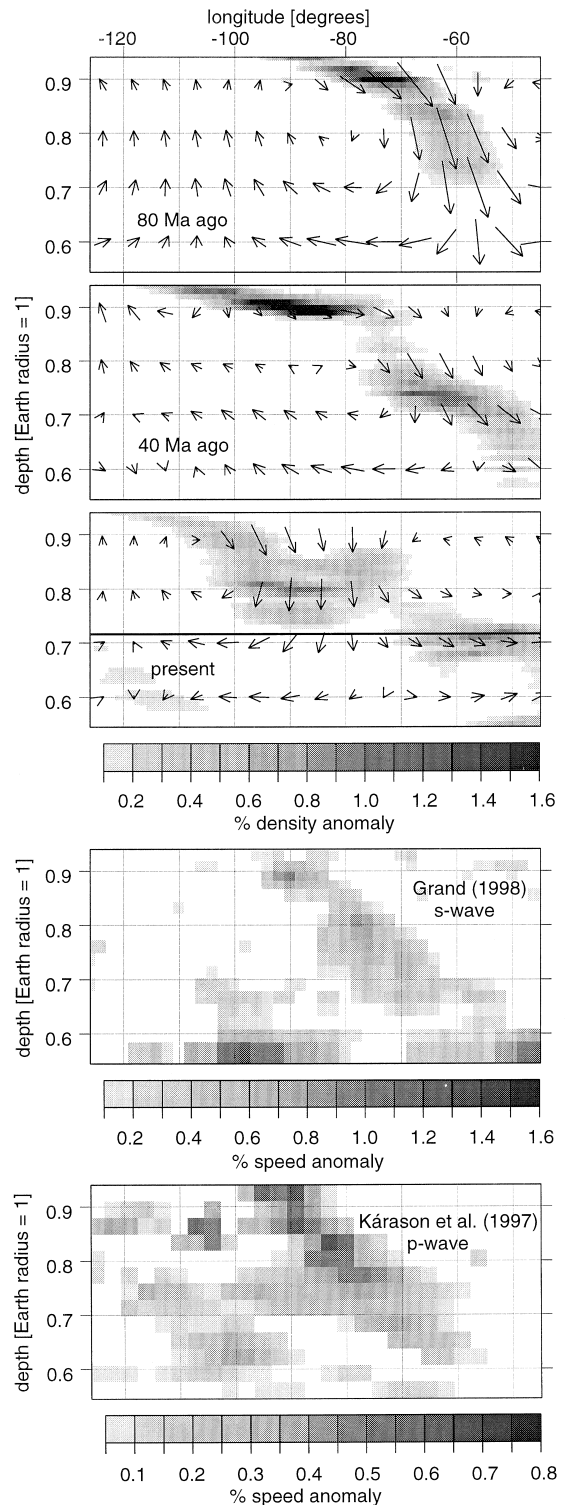


Fig. 7. Predicted density anomalies and flow due to subduction at three different times, and seismic p- and s-wave anomalies under North America — vertical cross-section at 38°N. Length of arrows corresponds to total flow in 20 Ma; only positive anomalies are shown. A thick black line indicates where flow is displayed in Fig. 4.

a maximum beneath the northern part of South America (a). Also, all three models show a maximum beneath Indonesia (b). In many other places, the models show considerable differences, which can be due to a variety of reasons: The interpretation of seismic anomalies in terms of density anomalies is not obvious, because p- and s- wave anomalies do not correlate well everywhere, as seen in Fig. 6; the subduction history model used may be inaccurate in places; the mantle flow model used may be too simplistic.

In the next layer (1100–1700 km), the maximum beneath the Americas is further north — roughly beneath the Caribbean in all three models (c). The maximum of the anomaly corresponding to Thetys subduction is further west — roughly beneath India in all three models (d). Again, the models disagree in other areas for the reasons mentioned above.

In the lower part of lower mantle, the predicted density anomalies remain in similar areas (below the Thetys region and around the Pacific) and an additional anomaly corresponding to the Mesozoic subduction between Izanagi and Farallon plates in the Northern Pacific (e) becomes prominent. Also, as a general feature, when going down in the mantle, the predicted anomalies become more patchy and less linear features. Comparison with seismic anomalies becomes even more difficult in the lowermost two layers: p- and s-wave anomalies look considerably different, which may be due to chemical heterogeneities (Kennett et al., 1998). The interpretation of seismic anomalies in terms of density anomalies therefore becomes less obvious. Also, the lowermost mantle must contain the remains of slabs subducted earlier than 120 Ma ago, which are not included in the model. Especially in the lowermost layer, we cannot expect that the model would predict all density anomalies. For example, although the predicted density anomaly beneath Asia extends further west than the locations of subduction during the past 120

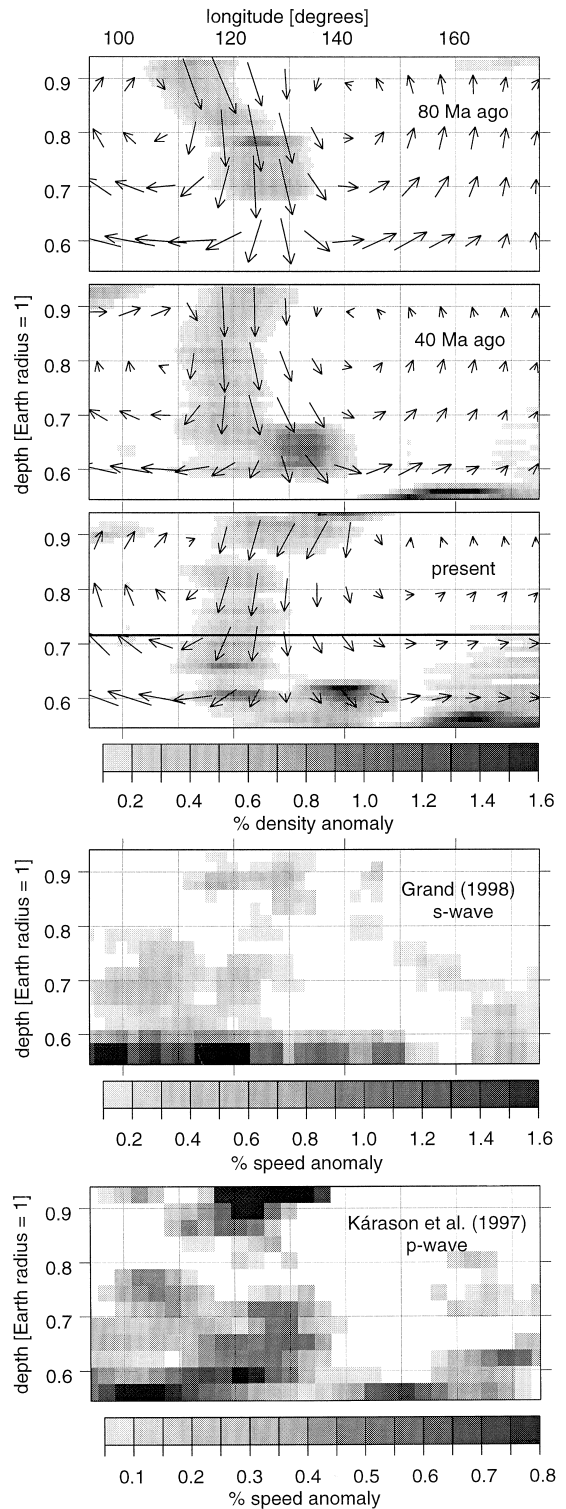


Fig. 8. Predicted density anomalies and flow due to subduction at three different times, and seismic p- and s-wave anomalies under East Asia — vertical cross-section at 38°N. Length of arrows corresponds to total flow in 20 Ma; only positive anomalies are shown. A thick black line indicates where flow is displayed in Fig. 4.

Ma, the anomaly seen in both tomographic models beneath Asia is considerably larger in extent and stretches even further west (f). This is most likely due to earlier subduction, as discussed by van der Voo et al. (1999).

3.3. Cross-sections through mantle

In the following, some cross-sections through the flow and density fields are shown: The regions displayed are on the surface of a cone, but they are mapped on to rectangles for convenience. The cross-sections only show vertical and east–west component of the flow, although flow calculations are done in three dimensions in spherical geometry.

A cross-section beneath North America is shown in Fig. 7, because the eastward dipping positive anomaly in both p- and s-wave speed has been one of the first strong evidences for slabs penetrating into the lower mantle (Grand, 1994). Here, it is therefore tested whether such a feature can be reproduced. The calculated density anomaly is in a similar location and has a similar shape: it also dips eastward, however, it is not as straight and dips less steeply. This might indicate that in this region the model somewhat underpredicts the slab sinking speed. The panel at 40 Ma ago shows the effect of the phase boundary in the calculations: Slabs pile up at the Spinel–Perovskite transition before they eventually penetrate into the lower mantle.

Fig. 8 shows a cross-section beneath East Asia. Again, the prediction and the tomographic images show an anomaly in a similar region and of similar shape: beginning in the upper mantle beneath Japan ($\sim 140^\circ\text{E}$) it stretches further west across the transition zone, and is more or less vertical in the lower mantle, going all the way to the CMB. Again, especially in the lowermost mantle, the predicted anomaly is not as extensive as observed, as the model does not include subduction earlier than 120 Ma. In this

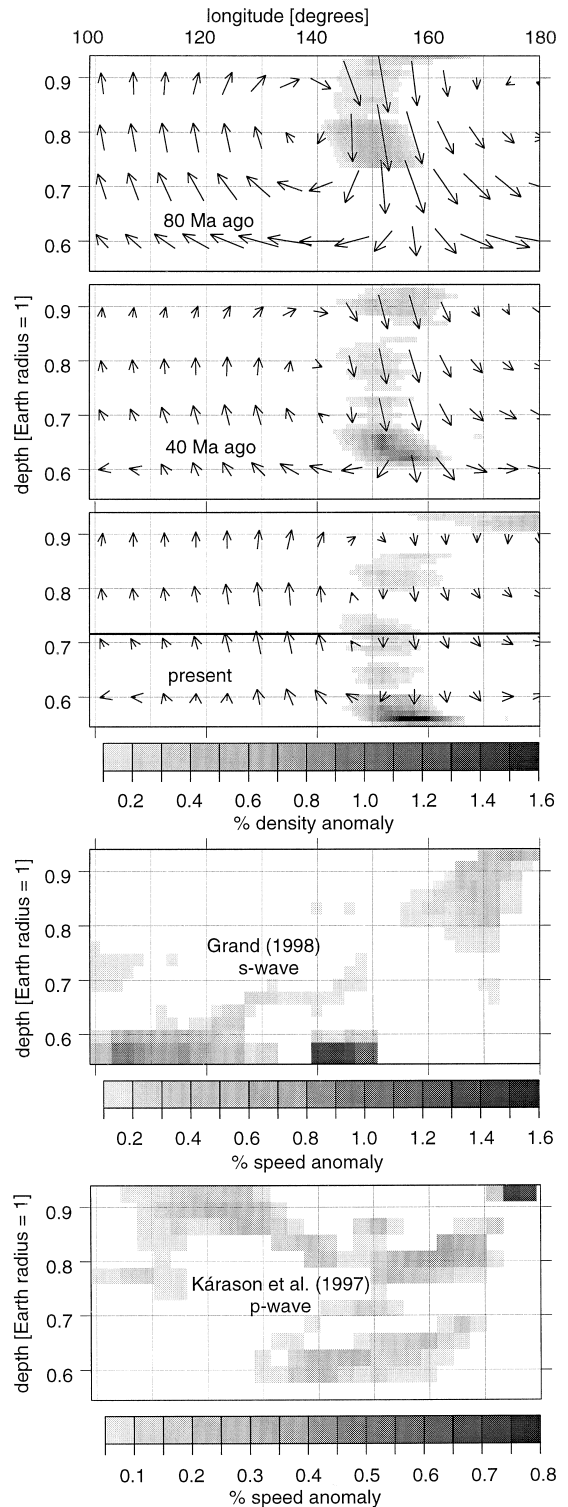


Fig. 9. Predicted density anomalies and flow due to subduction at three different times, and seismic p- and s-wave anomalies under Australia — vertical cross-section at 38°S . Length of arrows corresponds to total flow in 20 Ma; only positive anomalies are shown. A thick black line indicates where flow is displayed in Fig. 4.

region, the calculated effect of the phase transition is very small.

Finally, Fig. 9, showing a cross-section south of Australia, rather serves to indicate problems still to be overcome: Here, the tomographic models do not agree well, and the predicted density anomaly does not resemble either of them.

4. Slab distribution and the geoid

The theory relating mantle density heterogeneities and geoid has been developed by Richards and Hager (1984) and Ricard et al. (1984). Hager (1984) showed that a good fit to the geoid at spherical harmonic degrees 4–9 can be achieved if these density anomalies are inferred from the locations of subducted slabs. More recently, Ricard et al. (1993) were able to explain 73% of the first eight spherical harmonic degrees of the geoid, using a subduction history model. Both studies indicated a significant viscosity increase with depth (factor 30–100). Here, geoid kernels are computed with the method described by Panasyuk et al. (1996); the geoid is computed by convolving these kernels with the density anomaly inferred from slabs. There is a slight inconsistency in this procedure, as the geoid kernels were computed for a “free” upper boundary (although with a lithosphere 15 times more viscous than the mantle beneath), whereas the flow was calculated with the given plate motions as boundary condition. The boundary condition for the geoid was chosen because in this way the best fit can be achieved, as was previously noted (e.g., Thoraval and Richards, 1997). However, the inconsistency is not a serious one, as the results do not depend much on the assumed boundary condition. Even for a fixed surface boundary condition (i.e., zero plate motions as boundary condition for the flow, but the same slab input model) results look rather similar. Because of the low viscosity in the uppermost mantle, in the model plate motions are not strongly coupled to flow in the lower mantle, and motion of the slabs in the lower mantle depends mostly on the density anomaly of the slabs themselves and not much on the boundary condition. In Fig. 10, predicted and observed geoid are compared. There is good visual agreement in essential features: localized geoid highs over Indone-

sia (g) and South America (h), and a rather broad geoid high over Africa (i), geoid lows over northeastern North America (j), Siberia (k), the Indian Ocean (l), and Antarctica (m).

A more qualitative comparison can also be made directly between the slab distribution (Fig. 5) and the geoid: Slabs primarily in the lower mantle (such as below the south of India (n), central Siberia (o), Arctic Canada (p)) tend to be associated with geoid lows, whereas slabs primarily in the upper mantle (such as below New Guinea and surroundings (q), South America (r)) tend to be associated with geoid highs. Again, this points toward geoid kernels that are negative in the lowermost part of the mantle and positive in the upper part. The viscosity structure used here yields geoid kernels that show these characteristics at least for low spherical harmonic degrees. Predicted and observed geoid have similar magnitude, however, predicted geoid highs are higher than observed, predicted lows are not as low as observed. One reason for this discrepancy may be that geoid kernels ought to be less positive in the upper mantle and more negative in the lower mantle than the ones used here.

No attempt was made to optimize the fit to the geoid, with a more systematic search through parameter space. This would be beyond the scope of this paper, especially since this model does not include all density anomalies expected in the mantle: subducted slabs originate at the upper thermal boundary layer of the mantle, but there is also a lower thermal boundary layer that presumably gives rise to density heterogeneities in the form of mantle plumes. Because of higher viscosities in the lowermost mantle, it can be expected that plume conduits in the lowermost mantle are significantly thicker than closer to the surface. If, as in this model, geoid kernels are negative in the lowermost mantle at low spherical harmonic degrees, a high number of plumes per area will correspond to geoid highs at low spherical harmonic degrees. The observed distribution of hotspots and calculations of the shape of plume conduits (Steinberger, 2000) suggest that plume conduits in the lowermost mantle are particularly frequent under southern Africa and the South Central Pacific, which are in fact regions where the predicted geoid is, on a large scale, lower than observed. A positive correlation of the residual geoid (after subtracting the ef-

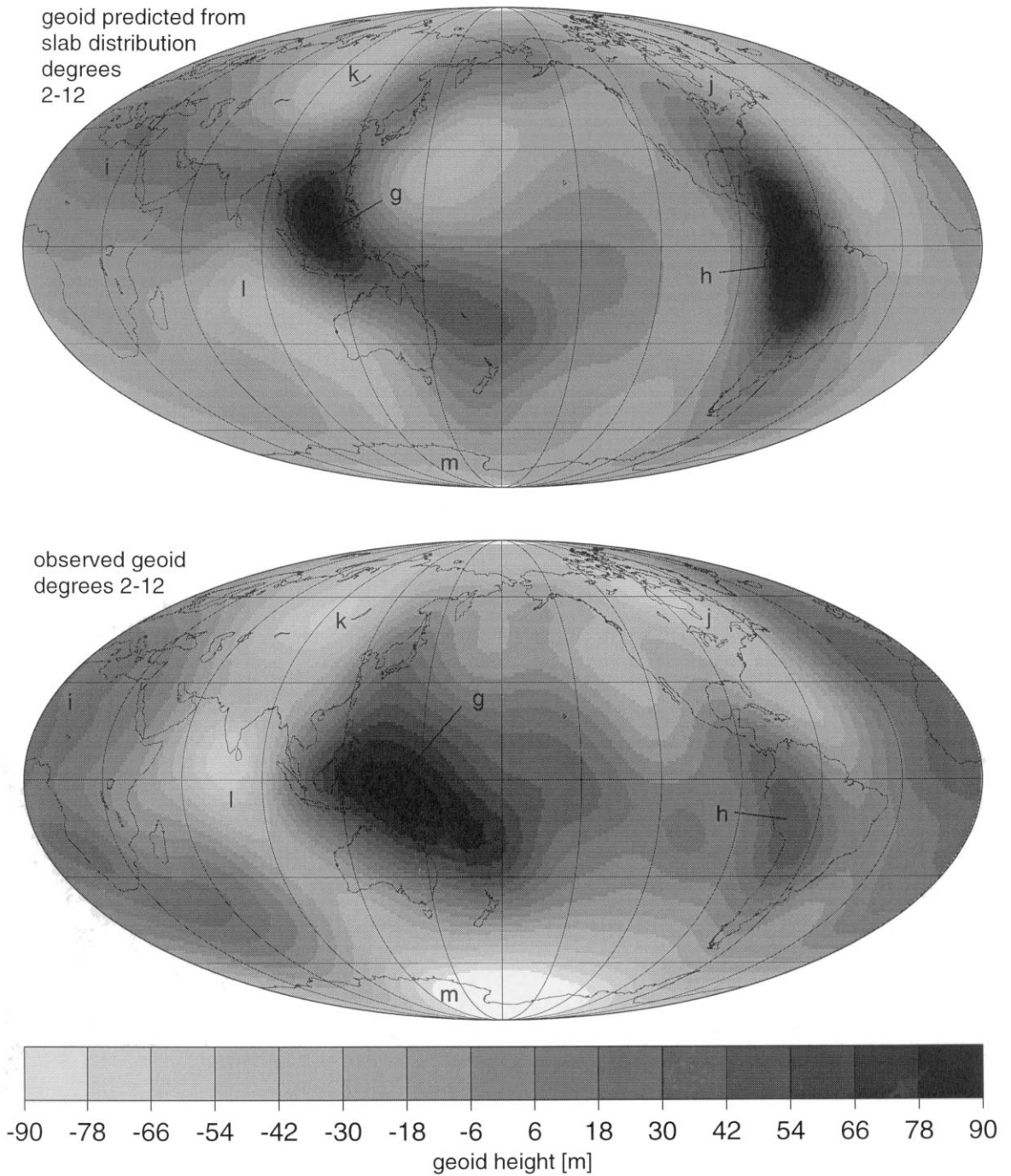


Fig. 10. Geoid “predicted” by convolving the calculated density anomaly due to subducted slabs with the kernels shown in Fig. 2. The observed geoid is shown for comparison. Letters (g,h,i,j,k,l,m) indicate places mentioned in text.

fects of subducted slabs) with the hotspot distribution has also been previously reported (e.g., Richards et al., 1988).

5. Conclusions

The results presented here do not differ dramatically from previous results. The average sinking speeds that were determined here are similar to what previously has been assumed. In most cases, lateral motion of slabs was found to be small, as shown in Fig. 11, thus largely justifying the assumption of vertical sinking that was used in some previous models. Lateral variations of sinking speed are, however, significant: The fastest sinking speeds result, where a lot of anomalous slab mass is subducted in the same area (i.e., without much trench migration). Fig. 4 shows the present maxima of sinking speed in the mid-mantle beneath China/South East Asia (s), the Caribbean (t), and the Scotia Sea (u).

In regions where the sinking speed has been fast, the model predicts that slabs subducted during the past 120 Ma have already sunk close to the CMB and spread laterally: Examples can be seen in Fig. 6 beneath Asia (f), the northern Pacific (e), and the Atlantic east of the Caribbean (v), as well as the

South Atlantic (w). In these areas, strong positive anomalies are predicted in the lowermost mantle, without subduction having occurred immediately above in the slab input model (Fig. 1). In accordance, both p- and s-wave models show large positive anomalies in the same region beneath Asia (f), and positive anomalies in a similar region beneath the northern Pacific (e); the s-wave model also has positive anomalies in the same two regions beneath the Atlantic (v) and (w). A rather large offset between subduction locations and slab location in the lowermost mantle is also predicted in the Indian ocean (n). Again, there are positive p- and s-wave anomalies close to where the slabs are predicted.

Both tomographic models also have some localized strong negative velocity anomalies (not shown), which are most likely unrelated to subduction. Additionally, the tomographic models have strong positive anomalies in some regions of the lowermost mantle where none are predicted, and which are likely due to earlier subduction. A significant shortcoming of this and other slab models is that the models of plate motion history and hence subduction used start 120 or 180 Ma ago. Our knowledge of the history of plate motion before that is not very good, and even the model used after 120 Ma, is probably wrong in some places. Fortunately, it may not be necessary to know subduction history accurately much earlier than about 150 Ma ago, as the results of Bunge et al. (1998) reveal a 150-Ma time scale for generating thermal heterogeneity in the mantle. The high-resolution tomographic images can now help to further constrain models of plate motion and subduction history; an example shown here concerns the subduction zone in the Northern Pacific, between Izanagi and Farallon plates, implied by Mesozoic plate reconstructions. The location of this subduction zone is not well constrained by plate reconstructions alone and the good agreement between predicted and observed anomalies (e) in that region helps to confirm the location. A more satisfactory approach than using a given subduction history model, as done here and in most previous studies, would be to vary plate reconstructions within their uncertainties and test which model best predicts tomography. Such an approach was taken by Gurnis et al. (1998) for a particular region; to do this on a global scale will be a considerable interdisciplinary research effort and is

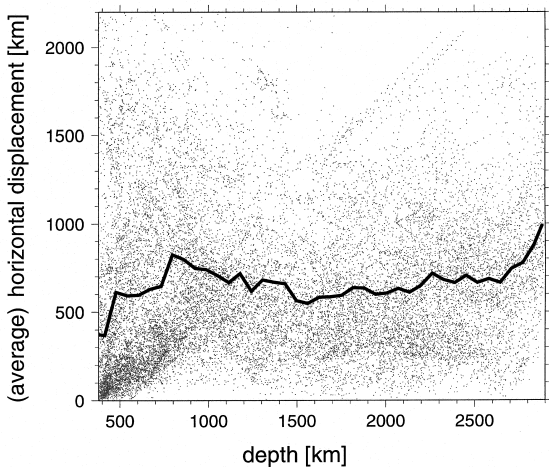


Fig. 11. Horizontal displacement of subducted slab particles between their initial location at depth 380 km and their present location. Each gray dot corresponds to one slab particle. The black line shows the average displacement of particles in spherical shells of thickness 0.01 Earth radii.

beyond the scope of the present paper, which is mainly intended to demonstrate the feasibility of such an effort.

The slab model does not strongly depend on details of the viscosity structure chosen. It can only be inferred that the average viscosity of the lower mantle must not be much less than about 10^{22} Pa. For the viscosity structure chosen, which reaches a value of $4 \cdot 10^{22}$ Pa in the lower mantle, slabs have on average sunk into the lower half of the lower mantle after about 100 Ma, but some slabs come close to the CMB already after about 60 Ma (see Fig. 3). For a viscosity much lower than that, model results show slabs reaching the lowermost mantle faster and subsequently spreading out close to the CMB, before they would presumably get thermally equilibrated — a result not in agreement with the observation that positive lowermost mantle seismic anomalies tend to be beneath areas of Mesozoic subduction and not much displaced laterally. If, on the other hand, a viscosity contrast much higher than 100 between upper and lower mantle is chosen, predictions of the geoid become less satisfactory. Although there are still considerable differences, a consensus between various current models of mantle viscosity, inferred from models of postglacial rebound and the geoid (e.g., Mitrovica and Forte, 1997; Lambeck and Johnston, 1998), and from hotspot motion (Richards, 1991; Corrieu and Ricard, 1998; Steinberger and O'Connell, 1998) begins to emerge. All those models indicate a significant viscosity increase with depth, with absolute viscosity in the upper mantle typically a few times 10^{20} Pa and lower mantle viscosity of the order of 10^{22} Pa or more. The viscosity model used here is in agreement with these general features.

Acknowledgements

Special thanks goes to Svetlana Panasyuk for providing the MATLAB code to calculate geoid kernels, and to Steve Grand and Rob van der Hilst for sharing their most recent tomographic models via anonymous ftp. A substantial part of this work was done during a postdoctoral fellowship at Academia Sinica (Taiwan). Some preliminary work was done with Rick O'Connell, who also provided various

FORTRAN routines and datasets for past plate motions and geometries, and whom I wish to thank for continuing encouragement to pursue this work. Further information and suggestions were given by Art Calderwood, Gabi Marquart, Harro Schmeling, Manuela Tetzlaff and Catherine Thoraval. Comments by Yanick Ricard and an anonymous reviewer are appreciated. Figures were prepared using GMT graphics (Wessel and Smith, 1995).

References

- Akaogi, M., Ito, E., 1999. Calorimetric study on majorite–perovskite transition in the system $\text{Mg}_4\text{Si}_4\text{O}_{12}$ – $\text{Mg}_3\text{Al}_2\text{Si}_3\text{O}_{12}$: transition boundaries with positive pressure–temperature slopes. *Phys. Earth Planet. Inter.* 114, 129–140.
- Akaogi, M., Ito, E., Navrotsky, A., 1989. Olivine-modified spinel–spinel transitions in the system Mg_2SiO_4 – Fe_2SiO_4 : calorimetric measurements, thermochemical calculations, and geophysical application. *J. Geophys. Res.* 94, 15671–15685.
- Bunge, H.-P., Richards, M.A., Lithgow-Bertelloni, C., Baumgardner, J.R., Grand, S.P., Romanowicz, B.A., 1998. Time scales and heterogeneous structure in geodynamic Earth models. *Science* 280, 91–95.
- Chopelas, A., Boehler, R., 1989. Thermal expansion measurements at very high pressure, systematics, and a case for a chemically homogeneous mantle. *Geophys. Res. Lett.* 16, 1347–1350.
- Corrieu, V., Ricard, Y., 1998. Hotspots and mantle dynamics. *Geophys. J. Int.*, submitted.
- Gordon, R.G., Jurdy, D., 1986. Cenozoic global plate motions. *J. Geophys. Res.* 91, 12389–12406.
- Grand, S.P., 1994. Mantle shear structure beneath the Americas and surrounding Oceans. *J. Geophys. Res.* 99, 11591–11621.
- Grand, S.P., van der Hilst, R.D., Widiyantoro, S., 1997. Global seismic tomography: a snapshot of convection in the Earth. *GSA Today* 7, 1–7.
- Gurnis, M., 1993. Phanerozoic marine inundation of continents driven by dynamic topography above subducting slabs. *Nature* 364, 589–593.
- Gurnis, M., Müller, R.D., Moresi, L., 1998. Dynamics of Cretaceous vertical motion of Australia and the Australian–Antarctic discordance. *Science* 279, 1499–1504.
- Hager, B.H., 1984. Subducted slabs and the geoid: constraints on mantle rheology and flow. *J. Geophys. Res.* 89, 6003–6015.
- Hager, B.H., O'Connell, R.J., 1979. Kinematic models of large-scale mantle flow. *J. Geophys. Res.* 84, 1031–1048.
- Hager, B.H., O'Connell, R.J., 1981. A simple global model of plate dynamics and mantle convection. *J. Geophys. Res.* 86, 4843–4867.
- Kárason, H., van der Hilst, R.D., Creager, K., 1997. Improving seismic models of global p-wave speed by the inclusion of core phases (abstract). *EOS Trans AGU* 78 (46), F17, Fall Meet. Suppl.

- Karato, S., 1993. Importance of anelasticity in the interpretation of seismic tomography. *Geophys. Res. Lett.* 20, 1623–1626.
- Kennett, B.L.N., Widiyantoro, S., van der Hilst, R.D., 1998. Joint seismic tomography for bulk sound and shear wave speed in the Earth's mantle. *J. Geophys. Res.* 103, 12469–12493.
- Lambeck, K., Johnston, P., 1998. The viscosity of the mantle: evidence from analyses of glacial-rebound phenomena. In: Jackson, I. (Ed.), *The Earth's Mantle*. Cambridge Univ. Press, pp. 461–502.
- Li, X.D., Romanowicz, B., 1996. Global mantle shear-velocity model developed using nonlinear asymptotic coupling theory. *J. Geophys. Res.* 101, 22245–22272.
- Lithgow-Bertelloni, C., Richards, M.A., 1998. The dynamics of Cenozoic and Mesozoic plate motions. *Rev. Geophys.* 36, 27–78.
- Lithgow-Bertelloni, C., Richards, M.A., Ricard, Y., O'Connell, R.J., Engebretson, D.C., 1993. Toroidal–poloidal partitioning of plate motions since 120 Ma. *Geophys. Res. Lett.* 20, 375–378.
- Mitrovica, J.X., Forte, A.M., 1997. Radial profile of mantle viscosity: results from the joint inversion of convection and postglacial rebound observables. *J. Geophys. Res.* 102, 2751–2769.
- Panasjuk, S.V., Hager, B.H., Forte, A.M., 1996. Understanding the effects of mantle compressibility on geoid kernels. *Geophys. J. Int.* 124, 121–133.
- Parsons, B., Sclater, J.G., 1977. An analysis of the variations of ocean floor bathymetry with age. *J. Geophys. Res.* 82, 803–827.
- Ricard, Y., Fleitout, L., Froidevaux, C., 1984. Geoid heights and lithospheric stresses for a dynamic Earth. *Ann. Geophys.* 2, 267–286.
- Ricard, Y., Richards, M.A., Lithgow-Bertelloni, C., LeStunff, Y., 1993. A geodynamic model of mass heterogeneity. *J. Geophys. Res.* 98, 21895–21909.
- Richards, M.A., 1991. Hotspots and the case for a high viscosity lower mantle. In: Sabadini, R., Lambeck, K. (Eds.), *Glacial Isostasy, Sea Level and Mantle Rheology*. Kluwer Academic Publishing, Dordrecht, pp. 571–587.
- Richards, M.A., Engebretson, D.C., 1992. Large-scale mantle convection and the history of subduction. *Nature* 355, 437–440.
- Richards, M.A., Hager, B.H., 1984. Geoid anomalies in a dynamic Earth. *J. Geophys. Res.* 89, 5987–6002.
- Richards, M.A., Hager, B.H., Sleep, N.H., 1988. Dynamically supported geoid highs over hotspots: observation and theory. *J. Geophys. Res.* 93, 7690–7708.
- Steinberger, B., 2000. Plumes in a convecting mantle: models and observations for individual hotspots. *J. Geophys. Res.*, in press.
- Steinberger, B.M., O'Connell, R.J., 1998. Advection of plumes in mantle flow: implications for hotspot motion, mantle viscosity and plume distribution. *Geophys. J. Int.* 132, 412–434.
- Su, W., Woodward, R.L., Dziewonski, A.M., 1994. Degree 12 model of shear velocity heterogeneity in the mantle. *J. Geophys. Res.* 99, 6945–6980.
- Thoraval, C., Richards, M.A., 1997. The geoid constraint in global geodynamics: viscosity structure, mantle heterogeneity models and boundary conditions. *Geophys. J. Int.* 131, 1–8.
- van der Hilst, R.D., Widiyantoro, S., Engdahl, E.R., 1997. Evidence for deep mantle circulation from global tomography. *Nature* 386, 578–584.
- van der Voo, R., Spakman, W., Bijwaard, H., 1999. Mesozoic subducted slabs under Siberia. *Nature* 397, 246–249.
- Wessel, P., Smith, W.H.F., 1995. New version of the generic mapping tools released. *EOS Trans. AGU* 76, 329.